Single-crystalline PbTe film growth through reorientation

Please check the document version of this publication:

• A submitted manuscript is the version of the article upon submission and before peer-review. There can be important differences between the submitted version and the official published version of record. People interested in the research are advised to contact the author for the final version of the publication, or visit the DOI to the publisher's website.
• The final author version and the galley proof are versions of the publication after peer review.
• The final published version features the final layout of the paper including the volume, issue and page numbers.

Link to publication

Single-crystalline PbTe film growth through reorientation

Jason Jung [1,*] Sander G. Schellingerhout [1,*] Orson A. H. van der Molen [1,*] Wouter H. J. Peeters [1]
Marcel A. Verheijen [1,2] and Erik P. A. M. Bakkers [1,†]

[1]*Department of Applied Physics, Eindhoven University of Technology, 5600 MB Eindhoven, The Netherlands*
[2]*Eurofins Materials Science Netherlands BV, 5656 AE Eindhoven, The Netherlands*

Heteroepitaxy enables the engineering of novel properties, which do not exist in a single material. Two principal growth modes are identified for material combinations with a large lattice mismatch, Volmer-Weber, and Stranski-Krastanov. Both lead to the formation of three-dimensional islands, hampering the growth of flat defect-free thin films. This limits the number of viable material combinations. Here, we report a distinct growth mode found in molecular beam epitaxy of PbTe on InP initiated by pregrowth surface treatments. Early nucleation forms islands analogous to the Volmer-Weber growth mode, but film closure exhibits a flat surface with atomic terracing. Remarkably, despite multiple distinct crystal orientations found in the initial islands, the final film is single crystalline. This is possible due to a reorientation process occurring during island coalescence, facilitating high quality heteroepitaxy despite the large lattice mismatch, difference in crystal structures, and diverging thermal expansion coefficients of PbTe and InP. This growth mode offers a new strategy for the heteroepitaxy of dissimilar materials and expands the realm of possible material combinations.

I. INTRODUCTION

Heteroepitaxy has been a staple of modern material science enabling a wide variety of techniques, such as band alignment tuning and surface passivation [1], crystal structure transfer [2], superlattices [3], strain engineering [4], and virtual substrates [5]. Strictly two-dimensional layer-by-layer growth ensues if adatoms are more strongly bound to the substrate than to each other [6]. For the heteroepitaxy of dissimilar materials, this is generally not possible [7]. Instead, if the adatoms are more strongly bound to each other than to the substrate, they follow the Volmer-Weber growth mode with the formation of three-dimensional islands [8]. Alternatively, in the intermediate Stranski-Krastanov case, initial layer-by-layer growth occurs until a critical thickness is reached where island growth ensues [9]. The two latter options lead to a three-dimensional surface topography with a high defect density [10–12]. This can be detrimental to the desired material characteristics or geometry, limiting the viable material combinations.

A prime example for a research field dependent on artificially structured materials with stringent quality requirements is topological quantum computation. Here, inherently fault-tolerant qubits have been proposed, based on the non-Abelian braiding statistics exhibited by Majorana bound states [13–16]. Suitable solid-state systems rely heavily on deliberate material design with proposals suggesting the use of semiconductor nanowire networks on an electrically isolating substrate, partially coupled to epitaxially grown superconducting islands [17–20]. Despite significant advances in the fabrication of the heterostructures [21–25], a definite proof of the existence of Majorana bound states is lacking. A major challenge is posed by material limitations causing disorder, e.g., surface roughness, charge impurities, point defects, atomic vacancies, patterning imperfections, or geometric restrictions [26–29]. The ability to reduce this disorder is critical for the development of Majorana qubits and solid-state based quantum technologies more broadly, making high quality heteroepitaxy imperative.

In this paper, we explore the molecular beam epitaxy of PbTe on InP (111)A substrates. The lead salt is an attractive material choice for topological quantum computation [30–42], suppressing disorder due to the screening of charged impurity scattering, resulting from the large dielectric constant [43,44]. InP is a suitable substrate due to the insulating properties, availability, and well-developed processing schemes. The growth initially mirrors the Volmer-Weber model, forming islands that, subsequently, coalesce, percolate, and finally, in response to a pregrowth surface treatment, form a closed film exhibiting a terrace-stepped surface. An involved crystal reorientation process facilitates the growth of large single-crystalline PbTe films regardless of the significant lattice mismatch, different crystal structure, and diverging thermal expansion coefficient between growth and substrate. Reorientation processes have previously only been shown in metals compensating small-angle mismatches between islands of about 1° [45]. High quality growth on a comparable material combination has been reported, however, no reorientation process was observed as initial islands exhibited only one epitaxial orientation upon surface treatments [46]. Understanding and exploiting the described growth mechanism can open paths

---

*These authors contributed equally to this work.
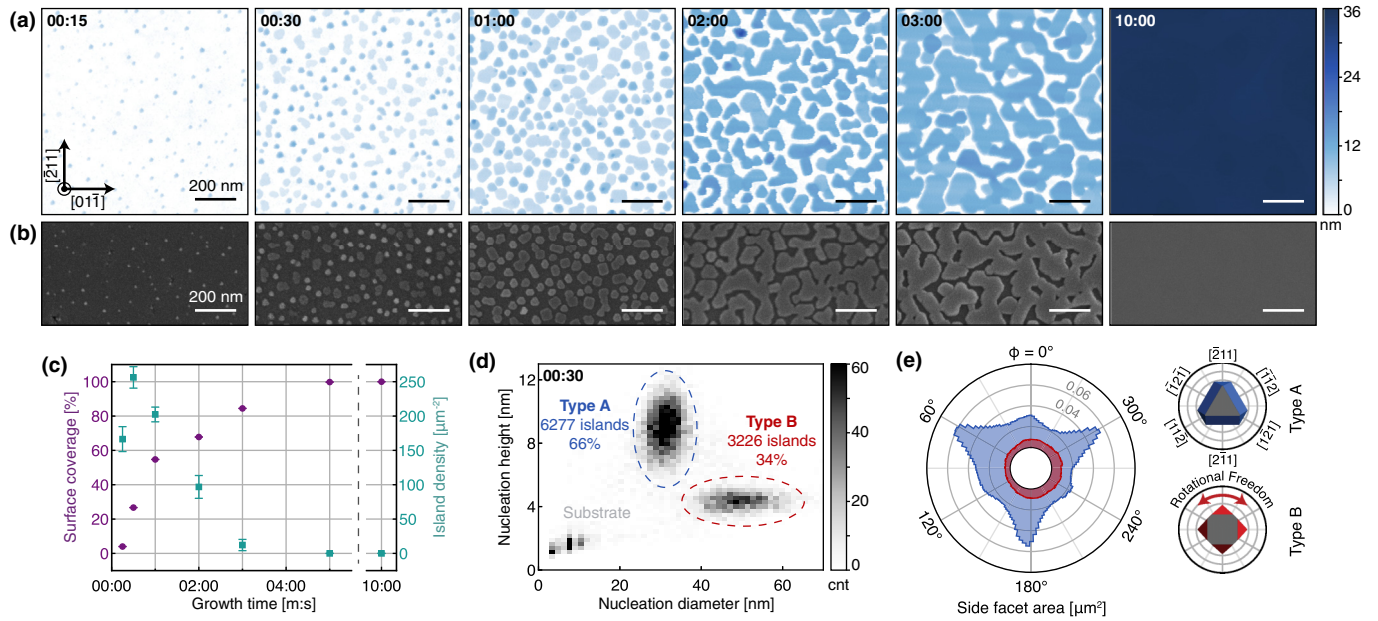†e.p.a.m.bakkers@tue.nl

FIG. 1. PbTe layer formation. (a) AFM scans depict the growth stages from initial island formation, to their coalescence, and the development of a closed layer. The in-plane crystal directions of the InP substrate are indicated in the first panel and kept consistent throughout. (b) SEM micrographs of the same samples. (c) Island density (cyan) and surface coverage (purple) plotted over growth time both extracted from AFM data. The number of islands reaches a maximum at 30 s after which the probability to form new nuclei decreases and islands begin to coalesce. At 3 min the film has percolated and is almost fully connected. The error bars show the standard deviation across 36 adjacent 1×1 μm areas. (d) A two-dimensional histogram compares diameter and height of islands taken from the AFM data at 30 s growth time. Two distinct types are discernible. (e) A polar histogram of the side facet area in dependence of the azimuthal angle ϕ taken from nuclei in the 30 s AFM data. A cutoff threshold is set for surfaces at polar angles $\theta \leqslant 20°$ relative to the substrate normal. The data indicate a preferential orientation of type A nuclei. This is not observed in type B nuclei, pointing towards a weak adhesive force between substrate and island. A Wulff construction of the two types suggests the involved facet directions, corresponding to peaks in the histogram.

to new high quality heterostructures involving dissimilar materials.

II. PbTe LAYER FORMATION

A time series, depicted in Figs. 1(a) and 1(b), explores the growth behavior of PbTe on (111)A InP substrates. Initially, discrete islands are formed, visible already at 15 s growth time. The islands, subsequently, expand both vertically and laterally until they begin to coalesce. The film has almost fully percolated at 3 min after which it forms a closed layer exhibiting atomic terracing which only forms in consequence of a pre-growth surface treatment (see Supplemental Material Fig. S1 [47]). This film formation behavior is summarized in Fig. 1(c) where island density and surface coverage are plotted over time. Initially, the observed increase of surface coverage is driven both by creation of new and expansion of existing islands. However, around 30 s, new nuclei stop forming and islands begin to coalesce, resulting in a decrease in the island density. The distributions of island height and diameter support the cessation of new island formation. This is shown for 30 s growth time as a two-dimensional histogram in Fig. 1(d). The lack of a tail into the small island heights and diameters imply a homogeneity in the age of the nuclei where the presence of a certain density of islands blocks the formation of new islands. This indicates a reasonable diffusion length of growth species over the InP substrate, as atoms impinging on the substrate are prevented from forming

a new island by diffusing to an existing one. Consequently, these islands compete for material. Figure 1(d) reveals not only a narrow spread for both displayed quantities, but also a bimodal distribution. This is a result of two distinct types of islands with different aspect ratios, hereafter referred to as type A (66%) and type B (34%). Analysis across different growth times confirms that islands of both types form before 15 s growth time and grow in both vertical and lateral directions with type-dependent rates (see Supplemental Material Fig. S2 [47]). Using surface normals extracted from the atomic force microscopy (AFM) data, the polar plot in Fig. 1(e) reveals the distribution of side facet orientations of the 30 s grown islands, separated by type. The presence of maxima indicates a preferential epitaxial orientation of type A islands with the corresponding facets indicated in the inset Wulff construction [51,52]. The absence of any preferred orientation in type B islands suggests by contrast an in-plane rotational freedom.

III. EPITAXIAL ORIENTATION OF ISLANDS

Transmission electron microscopy (TEM) analysis of the 30 s grown sample reveals three island types, each defined by a distinct epitaxial relation to the substrate. A representative high-resolution TEM image of the most frequent type A_1 is shown in Fig. 2(a). This type is characterized by a twinned epitaxial relation between PbTe and InP as confirmed by the micrograph's (FFT. This results in a $[\bar{2}11]_{InP,\perp}/[2\bar{1}\bar{1}]_{PbTe,\perp}$
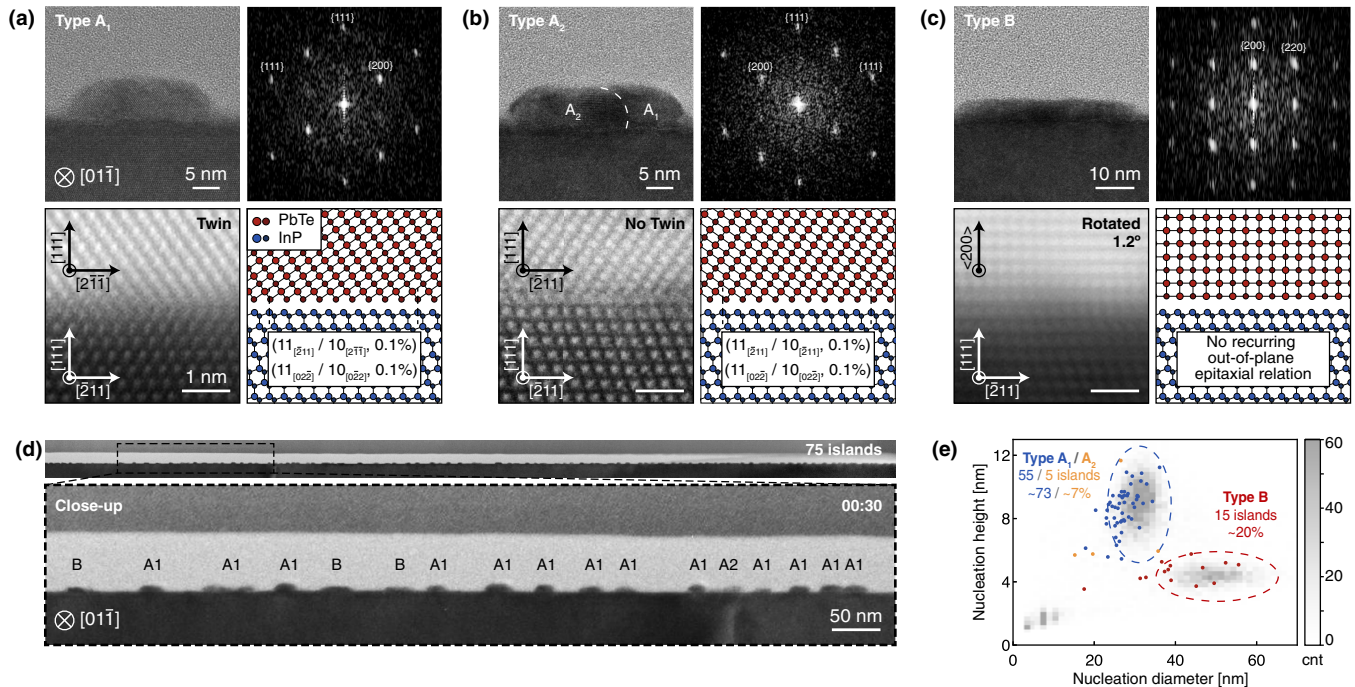
FIG. 2. Epitaxial orientation of islands. (a) and (c) Islands exhibit three types of epitaxial orientation to the substrate. For each type are shown, a representative TEM micrograph, the two-dimensional fast Fourier transform (FFT) of an aforementioned micrograph, a high-angle annular dark-field (HAADF) scanning TEM micrograph of an equivalent interface, and the corresponding structural model of the crystal lattice. The TEM micrograph of (b) shows two superimposed islands, each with their distinct type indicated. (d) Bright-field TEM micrograph of a cross section taken from the 30 s growth time sample shown in Fig. 1(a). A closeup displays islands and their type. (e) Height and diameter of the islands measured with TEM. Data are in line with the histogram from Fig. 1(d), which confirms the connection between epitaxial orientation and the island types found from AFM.

and $[02\bar{2}]_{InP,\parallel}/[0\bar{2}2]_{PbTe,\parallel}$ interface along the in-plane directions transverse and parallel to the depicted zone axis. A HAADF-scanning TEM image of an equivalent interface reveals the atomic planes of both crystal phases and establishes a structural model of the lattice. The large lattice mismatch of 10.1% is overcome through the formation of edge-type misfit dislocations at the InP-PbTe interface, breaking bonds in exchange for a reduction of strain. For type A_1, an $11_{[\bar{2}11]}/10_{[2\bar{1}\bar{1}]}$ lattice plane ratio is found in plane, leading to 0.1% residual mismatch in the corresponding ideal flat interface. The less-frequent type A_2 shown in Fig. 2(b) exhibits no interfacial twinning. The $[\bar{2}11]_{InP,\perp}/[\bar{2}11]_{PbTe,\perp}$ and $[02\bar{2}]_{InP,\parallel}/[02\bar{2}]_{PbTe,\parallel}$ crystal directions are a direct continuation of the substrate with an identical lattice plain ratio and residual mismatch as type A_1 due to the structural similarity. In contrast to both types A_i, type B changes out-of-plane crystal direction at the interface from [111] to ⟨200⟩. Despite this distinct out-of-plane direction, no preferential in-plane orientation can be found, suggesting a weak adhesive force between the substrate and this island type [53]. Due to this, no recurring lattice plain ratio or residual mismatch can be assigned to this island type. A bright-field TEM micrograph of the complete cross section with 75 islands is shown in Fig. 2(d). Several labeled islands can be seen in the closeup. In Fig. 2(e) the diameter and height values of islands found in the cross-sectional cut, measured via TEM, are compared to the AFM data presented in Fig. 1(e). Tip convolution effects during the AFM measurement likely lead to an overestimation of the island diameter, in addition to the uncertainties introduced

by the TEM projection. Despite these inherent inaccuracies, a close agreement between these measurement modalities is found, connecting the TEM-based epitaxial relation of the island types with the superior statistics of the AFM data.

IV. REORIENTATION UPON COALESCENCE

In light of the various crystal orientations present during the initial growth stages, it is of particular interest to study the mechanics leading to a closed film with atomically flat terraces. The stable lattice plane orientation throughout the growth (see Supplemental Material Fig. S3 [47]) enables their study through symmetric ω-2θ XRD scans. Figure 3(a) plots sections of the scattered x-ray intensity for increasing growth times. Fitting the XRD spectra with pseudo-Voigt functions allows for the identification of the isolated InP (111), PbTe (111), and PbTe (200) peaks and their higher-order reflections. The two PbTe peaks correspond to type A_i and type B epitaxy, respectively. No indications of other orientations can be found, confirming the absence of additional types (see Supplemental Material Fig. S4 [47]). The area under each peak is correlated with the probed volume of that crystal orientation [50]. Figure 3(b) compares the peak area of PbTe (222) and PbTe (200) with growth time as an indication of the crystal growth evolution. Each calculated area is normalized with the InP peak area to eliminate any influence originating from varying sample size and alignment. The first noticeable characteristic of the plot is the steady increase in the PbTe (222) volume. As expected, the same
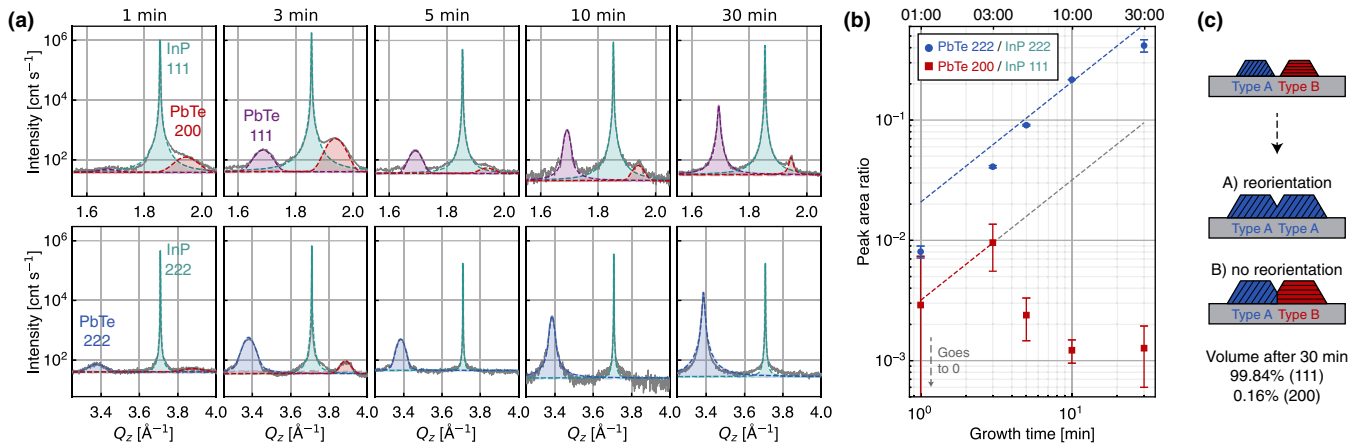
FIG. 3. Reorientation upon island coalescence. (a) Symmetric ω-2θ x-ray diffraction (XRD) scans of PbTe grown on InP substrates. The first- (top row) and second- (bottom row) order peaks are plotted for increasing growth times. (b) The peak area ratio between PbTe and InP is indicative of the probed crystal volume. Opposed to the continuously increasing (111)-oriented PbTe crystal volume, the (200)-oriented volume decreases by nearly an order of magnitude following 3 min growth time. This is suggestive of a crystal reorientation process of islands with diverging epitaxial relation, triggered upon coalescence. The remaining (200) signal at 30 min growth time implies that nearly all undergo this process, with $(0.16 \pm 0.06)\%$ of the film volume estimated to remain (200)-oriented (see Supplemental Material Fig. S4 [47]). (c) A schematic illustrating the suggested reorientation process. Upon coalescence, type *B* islands can adapt their crystallographic orientation.

behavior is found for PbTe (111) (see Supplemental Material Fig. S4 [47]). In contrast to this, following an initial increase, the probed (200) crystal volume decreases by nearly an order of magnitude. No new orientations appear in the XRD spectra, pointing towards a reorientation process of the initial type *B* nuclei into type A_i. Based on the growth time dependency, the reorientation likely takes place upon island coalescence up until the subsequent film percolation. A sketch of the proposed process is shown in Fig. 3(c). However, not all islands undergo this reorientation process as evident from the remaining PbTe (200) signal at 30 min growth time. This is supported by the continuously decreasing (200) peak width in Fig. 3(a), a sign of ongoing vertical growth of those grains. Together with the initial (200) area decrease, this excludes overgrowth of the nuclei as a possible explanation of the observed phenomena, and instead suggests the coexistence of a small volume fraction of $(0.16 \pm 0.06)\%$ remaining (200) type *B* grains at the PbTe growth front (see Supplemental Material Fig. S4 [47]). We note that this can likely be further optimized. Reciprocal space maps of asymmetric reflections distinguish twinned and nontwinned (111) PbTe layers and are used to quantify the ratio between type A_1 and type A_2 in the layer (see Supplemental Material Fig. S5 [47]). Already at 3 min growth time all (111)-oriented PbTe is found to be twinned relative to the InP substrate, i.e., only type A_1 remains. This is consistent with respective TEM observations [42]. Island orientation and morphology are governed by the interfacial and surface free energies. Additionally, there can be a bulk contribution in the form of strain energy, and contributions stemming from defects or grain boundaries. For reorientation to occur, it must both lead to a lower-energy state and not have too high of an energy barrier. The relative influence of the substrate on the islands is expected to decline over time as the surface-to-volume ratio decreases. As such, it is unlikely that the reorientation of islands occurs spontaneously as the islands grow. The introduction of grain boundaries between different island types is, therefore, identified as the most probable trigger for reorien-

tation. As the reorientation process occurs predominately to exclusively from type A_2 and *B* towards type A_1, the substrate interface plays a directing role in the reorientation, suggesting a minimal interfacial energy for type A_1 islands. It is difficult to overemphasize the importance of the reorientation process as it facilitates the heteroepitaxy of high-quality thin films on dissimilar substrates, in this case PbTe (111) on InP (111)*A*. In fact, the seemingly unfit substrate with its large lattice mismatch, different crystal structure, and diverging thermal expansion coefficient, are believed to lead to a weak adhesive force between substrate and growth, facilitating the reorientation process.

V. LAYER MOSAICITY

The crystal quality resulting from the reorientation process is assessed via TEM. A cross section of a selective area grown (SAG) $2 \times 2\,\mu m$ structure shows subtle contrast variations throughout the film. These become pronounced when imaged off zone axisas depicted in Fig. 4(a). Despite these boundaries and despite the film originating from many islands with various epitaxial orientations, the complete cross section has a single twinned epitaxial relation to the substrate, confirming the observations made in Fig. 3. This finding is supported by equivalent electron diffraction patterns taken across the complete segment (see Supplemental Material Fig. S6 [47]). A representative example is shown in Fig. 4(b). The contrast variations visible in Fig. 4(a) are identified as boundaries between slightly misoriented segments where the misorientation is a rotation around the surface normal of the substrate. The rotations are distributed between $0°$ and $0.5°$ and have a positive mean, indicating that in addition to individual variation, there is a common rotation relative to the substrate. The average relative rotation between neighboring segments is $0.2°$. This corresponds to a shift of one lattice plane about every 287 columns (about 185 nm in the PbTe crystal), and, therefore, amounts to,
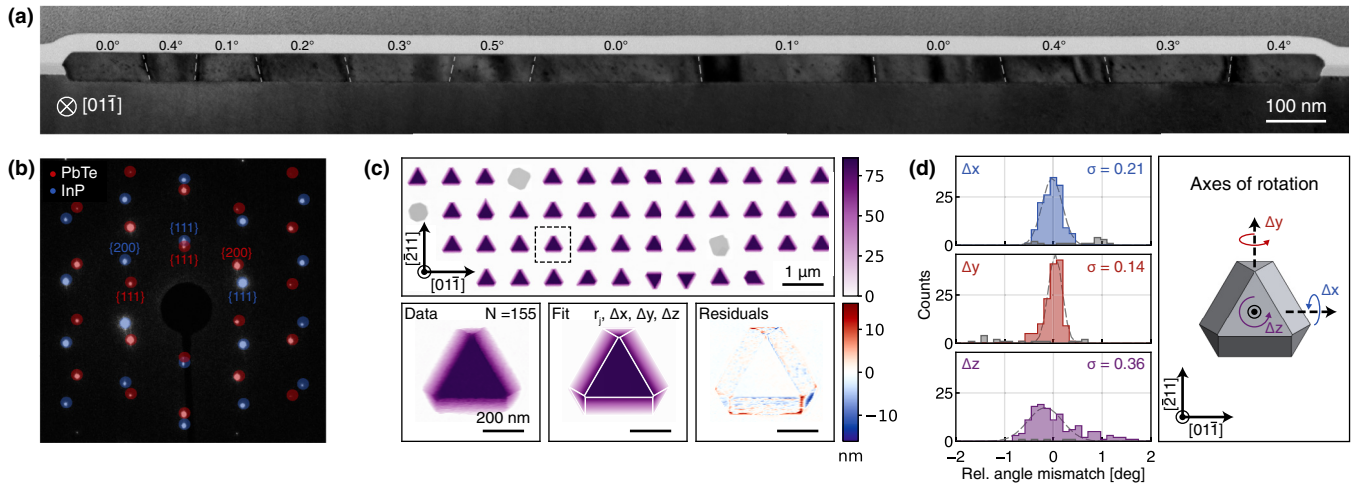
FIG. 4. Layer mosaicity. (a) Cross section of a 2×2 μm PbTe structure, captured via bright-field TEM. The image is taken off zone axis to emphasize contrast variations throughout the film originating from strain between merged segments (separated by dashed lines). The misalignment, i.e., the relative rotation around the substrate normal between each segment and the substrate is indicated. (b) Despite this, the complete PbTe segment is single crystalline as demonstrated by a representative diffraction pattern taken from a full data set (see Supplemental Material Fig. S6 [47]). (c) AFM scan of SAG structures grown from circular mask openings, showing well-defined {200} and {111} facets. Facet radii and three-axis rotation are fitted to each structure with a typical structure, corresponding fit, and residual shown in the bottom panels. (d) Distribution of rotations for each axis across 155 structures. Bad fits with a relative residual volume above 4% are plotted in gray. The axis definitions are shown in the right panel.

at most, a few planes offset over the length of each segment. This confirms that the PbTe films are single crystalline, accompanied by slight mosaicity. The segment boundaries are not a result of incomplete reorientation between coalescing pairs of islands of different types. Based on the AFM data presented in Fig. 1, on average seven islands, of which two type B, combine to form a single segment of type A_1. This suggests that multiple islands combine and reorient to form a strain-free segment. To inspect the origin of the strain features, nanostructures were selectively grown from circular openings with a 200 nm diameter as shown in Fig. 4(c). Based on the segment dimensions visible in TEM, the structures are expected to consist on average of a single segment. As such, measurements of their orientations can be compared to segment orientations in films before their merging. The facets formed in the nanostructures belong to the {111} and {200} families and can be reproduced via Wulff construction [42]. Based on the crystal symmetry, a fitting function is defined and used to acquire both facet radii and misorientation in three axes of rotation. A representative fit is shown in the bottom panel of Fig. 4(c). A histogram over 155 fitted structures is depicted for each rotational axis in Fig. 4(d). The found standard deviation of the out-of-plane rotation Δz is 0.36°. This includes noise from imperfect facets, AFM measurement, and fitting and, therefore, gives an upper bound to the variation in structure orientations. The distribution suggests, that the origin of the strain features can be found in slight misalignments between meeting grains that have become too large in size to align completely.

VI. CONCLUSION

To summarize, we present a distinct growth mode facilitating high-quality heteroepitaxy of dissimilar materials by ex-

ample of PbTe on InP (111)A substrates. AFM measurements reveal the three-dimensional islands present in early stages of the growth, and the eventual formation of a closed film. Structural differences in the initial islands are attributed to three distinct epitaxial orientations. XRD scans following the, subsequent, growth stages expose a reorientation process, facilitating the formation of a predominantly single-crystalline film. A fascinating outcome, considering the initial differences in epitaxial orientation of the nuclei. Small-angle misalignment is detected between segments of the film leading to strain signatures exposed by off zone axis TEM. Nevertheless, our recent quantum experiments on selective area grown structures employing the same growth mechanism yield electron mobilities comparable to InSb and a coherence length exceeding any previously reported values on selective area grown networks, signifying the high crystal quality of the PbTe [42]. Future work will explore the heteroepitaxial growth of topological crystalline insulators, namely, SnTe and PbSnTe that are expected to exhibit comparable growth behavior.

The data supporting the findings of this paper are openly available in Ref. [54].

[1] L. J. Lauhon, M. S. Gudiksen, D. Wang, and C. M. Lieber, Epitaxial core-shell and coremultishell nanowire heterostructures, Nature (London) **420**, 57 (2002).

[2] E. M. T. Fadaly, A. Dijkstra, J. R. Suckert, D. Ziss, M. A. J. v. Tilburg, C. Mao, Y. Ren, V. T. v. Lange, K. Korzun, S. Kölling, M. A. Verheijen, D. Busse, C. Rödl, J. Furthmüller, F. Bechstedt, J. Stangl, J. J. Finley, S. Botti, J. E. M. Haverkort, and E. P. A. M. Bakkers, Direct-bandgap emission from hexagonal Ge and SiGe alloys, Nature (London) **580**, 205 (2020), 1911.00726.

[3] J. A. Mundy, C. M. Brooks, M. E. Holtz, J. A. Moyer, H. Das, A. F. Rébola, J. T. Heron, J. D. Clarkson, S. M. Disseler, Z. Liu, A. Farhan, R. Held, R. Hovden, E. Padgett, Q. Mao, H. Paik, R. Misra, L. F. Kourkoutis, E. Arenholz, A. Scholl *et al.*, Atomically engineered ferroic layers yield a room-temperature magnetoelectric multiferroic, Nature (London) **537**, 523 (2016).

[4] F. Schäffler, High-mobility Si and Ge structures, Semicond. Sci. Technol. **12**, 1515 (1997).

[5] Y. A. Bioud, A. Boucherif, M. Myronov, A. Soltani, G. Patriarche, N. Braidy, M. Jellite, D. Drouin, and R. Arés, Uprooting defects to enable high-performance IIIV optoelectronic devices on silicon, Nat. Commun. **10**, 4322 (2019).

[6] F. C. Frank and J. H. v. d. Merwe, One-dimensional dislocations. I. Static theory, Proc. R. Soc. London, Ser. A **198**, 205 (1949).

[7] C. J. Palmstrom, Epitaxy of dissimilar materials, Annu. Rev. Mater. Sci. **25**, 389 (1995).

[8] M. Volmer and A. Weber, Keimbildung in übersättigten Gebilden, Zeitschrift für Physikalische Chemie **119U**, 277 (1926).

[9] I. N. Stranski and L. Krastanow, Zur Theorie der orientierten Ausscheidung von Ionenkristallen aufeinander, Monatsh. Chem. **71**, 351 (1937).

[10] J. A. Floro, S. J. Hearne, J. A. Hunter, P. Kotula, E. Chason, S. C. Seel, and C. V. Thompson, The dynamic competition between stress generation and relaxation mechanisms during coalescence of Volmer-Weber thin films, J. Appl. Phys. **89**, 4886 (2001).

[11] Y.-W. Mo, D. E. Savage, B. S. Swartzentruber, and M. G. Lagally, Kinetic pathway in Stranski-Krastanov growth of Ge on Si(001), Phys. Rev. Lett. **65**, 1020 (1990).

[12] C. Teichert, Self-organization of nanostructures in semiconductor heteroepitaxy, Phys. Rep. **365**, 335 (2002).

[13] A. Y. Kitaev, Unpaired Majorana fermions in quantum wires, Phys.-Usp. **44**, 131 (2001).

[14] A. Kitaev, Fault-tolerant quantum computation by anyons, Ann. Phys. (NY) **303**, 2 (2003).

[15] C. Nayak, S. H. Simon, A. Stern, M. Freedman, and S. D. Das Sarma, Non-Abelian anyons and topological quantum computation, Rev. Mod. Phys. **80**, 1083 (2008).

[16] S. D. Sarma, M. Freedman, and C. Nayak, Majorana zero modes and topological quantum computation, npj Quantum Inf. **1**, 15001 (2015).

[17] R. M. Lutchyn, J. D. Sau, and S. Das Sarma, Majorana Fermions and a Topological Phase Transition in Semiconductor-Superconductor Heterostructures, Phys. Rev. Lett. **105**, 077001 (2010).

[18] Y. Oreg, G. Refael, and F. von Oppen, Helical Liquids and Majorana Bound States in Quantum Wires, Phys. Rev. Lett. **105**, 177002 (2010).

[19] T. Karzig, C. Knapp, R. M. Lutchyn, P. Bonderson, M. B. Hastings, C. Nayak, J. Alicea, K. Flensberg, S. Plugge, Y. Oreg, C. M. Marcus, and M. H. Freedman, Scalable designs for quasiparticle-poisoning-protected topological quantum computation with Majorana zero modes, Phys. Rev. B **95**, 235305 (2017).

[20] S. Plugge, A. Rasmussen, R. Egger, and K. Flensberg, Majorana box qubits, New J. Phys. **19**, 012001 (2017).

[21] W. Chang, S. M. Albrecht, T. S. Jespersen, F. Kuemmeth, P. Krogstrup, J. Nygård, and C. M. Marcus, Hard gap in epitaxial semiconductor-superconductor nanowires, Nat. Nanotechnol. **10**, 232 (2015).

[22] Ö. Gül, H. Zhang, F. K. d. Vries, J. v. Veen, K. Zuo, V. Mourik, S. Conesa-Boj, M. P. Nowak, D. J. v. Woerkom, M. Quintero-Pérez, M. C. Cassidy, A. Geresdi, S. Koelling, D. Car, S. R. Plissard, E. P. A. M. Bakkers, and L. P. Kouwenhoven, Hard superconducting gap in InSb nanowires, Nano Lett. **17**, 2690 (2017).

[23] F. Krizek, J. E. Sestoft, P. Aseev, S. Marti-Sanchez, S. Vaitiekėnas, L. Casparis, S. A. Khan, Y. Liu, T. Stankevič, A. M. Whiticar, A. Fursina, F. Boekhout, R. Koops, E. Uccelli, L. P. Kouwenhoven, C. M. Marcus, J. Arbiol, and P. Krogstrup, Field effect enhancement in buffered quantum nanowire networks, Phys. Rev. Mater. **2**, 093401 (2018).

[24] S. Heedt, M. Quintero-Pérez, F. Borsoi, A. Fursina, N. van Loo, G. P. Mazur, M. P. Nowak, M. Ammerlaan, K. Li, S. Korneychuk, J. Shen, M. A. Y. van de Poll, G. Badawy, S. Gazibegovic, N. de Jong, P. Aseev, K. van Hoogdalem, E. P. A. M. Bakkers, and L. P. Kouwenhoven, Shadow-wall lithography of ballistic superconductor-semiconductor quantum devices, Nat. Commun. **12**, 4914 (2021).

[25] T. Kanne, M. Marnauza, D. Olsteins, D. J. Carrad, J. E. Sestoft, J. de Bruijckere, L. Zeng, E. Johnson, E. Olsson, K. Grove-Rasmussen, and J. Nygård, Epitaxial Pb on InAs nanowires for quantum devices, Nat. Nanotechnol. **16**, 776 (2021).

[26] H. Pan and S. Das Sarma, Physical mechanisms for zero-bias conductance peaks in Majorana nanowires, Phys. Rev. Res. **2**, 013377 (2020).

[27] S. Das Sarma and H. Pan, Disorder-induced zero-bias peaks in Majorana nanowires, Phys. Rev. B **103**, 195158 (2021).

[28] B. D. Woods, S. Das Sarma, and T. D. Stanescu, Charge-Impurity Effects in Hybrid Majorana Nanowires, Phys. Rev. Appl. **16**, 054053 (2021).

[29] S. Ahn, H. Pan, B. Woods, T. D. Stanescu, and S. Das Sarma, Estimating disorder and its adverse effects in semiconductor majorana nanowires, Phys. Rev. Mater. **5**, 124602 (2021).

[30] G. Springholz, G. Bauer, and G. Ihninger, MBE of high mobility PbTe films and PbTe/$Pb_{1-x}Eu_xTe$ heterostructures, J. Cryst. Growth **127**, 302 (1993).

[31] G. Grabecki, J. Wróbel, T. Dietl, K. Byczuk, E. Papis, E. Kamińska, A. Piotrowska, G. Springholz, M. Pinczolits, and G. Bauer, Quantum ballistic transport in constrictions of n-PbTe, Phys. Rev. B **60**, R5133(R) (1999).

[32] G. Grabecki, J. Wróbel, T. Dietl, E. Papis, E. Kamińska, A. Piotrowska, A. Ratuszna, G. Springholz, and G. Bauer, Ballistic transport in PbTe-based nanostructures, Physica E **20**, 236 (2004).

[33] V. A. Chitta, W. Desrat, D. K. Maude, B. A. Piot, N. F. Oliveira, P. H. O. Rappl, A. Y. Ueta, and E. Abramof, Multivalley transport and the integer quantum Hall effect in a PbTe quantum well, Phys. Rev. B **72**, 195326 (2005).

[34] V. A. Chitta, W. Desrat, D. Maude, B. Piot, N. F. Oliveira Jr., P. Rappl, A. Ueta, and E. Abramof, Integer quantum Hall effect in a PbTe quantum well, Physica E **34**, 124 (2006).

[35] G. Grabecki, J. Wróbel, T. Dietl, E. Janik, M. Aleszkiewicz, E. Papis, E. Kamińska, A. Piotrowska, G. Springholz, and G. Bauer, PbTeA new medium for quantum ballistic devices, Physica E **34**, 560 (2006).

[36] M. Wuttig, V. L. Deringer, X. Gonze, C. Bichara, and J.-Y. Raty, Incipient metals: Functional materials with a unique bonding mechanism, Adv. Mater. **30**, 1803777 (2018).

[37] Z. Geng, Z. Zhang, F. Chen, S. Yang, Y. Jiang, Y. Gao, B. Tong, W. Song, W. Miao, R. Li *et al.*, Observation of Aharonov-Bohm effect in PbTe nanowire networks, Phys. Rev. B **105**, L241112 (2022).

[38] S. G. Schellingerhout, E. J. d. Jong, M. Gomanko, X. Guan, Y. Jiang, M. S. M. Hoskam, J. Jung, S. Koelling, O. Moutanabbir, M. A. Verheijen, S. M. Frolov, and E. P. A. M. Bakkers, Growth of PbTe nanowires by molecular beam epitaxy, Materials for Quantum Technology **2**, 015001 (2022).

[39] Z. Cao, D. E. Liu, W.-X. He, X. Liu, K. He, and H. Zhang, Numerical study of PbTe-Pb hybrid nanowires for engineering Majorana zero modes, Phys. Rev. B **105**, 085424 (2022).

[40] Y. Jiang, S. Yang, L. Li, W. Song, W. Miao, B. Tong, Z. Geng, Y. Gao, R. Li, F. Chen, Q. Zhang, F. Meng, L. Gu, K. Zhu, Y. Zang, R. Shang, Z. Cao, X. Feng, Q.-K. Xue, D. E. Liu *et al.*, Selective area epitaxy of PbTe-Pb hybrid nanowires on a lattice-matched substrate, Phys. Rev. Mater. **6**, 034205 (2022).

[41] S. C. t. Kate, M. F. Ritter, A. Fuhrer, J. Jung, S. G. Schellingerhout, E. P. A. M. Bakkers, H. Riel, and F. Nichele, Small charging energies and g-factor anisotropy in PbTe quantum dots, Nano Lett. **22**, 7049 (2022).

[42] J. Jung, S. Schellingerhout, M. Ritter, S. ten Kate, O. van der Molen, S. de Loijer, M. Verheijen, H. Riel, F. Nichele, and E. Bakkers, Selective area growth of PbTe nanowire networks on InP, Adv. Funct. Mater. **22**, 2208974 (2022).

[43] S. Yuan, H. Krenn, G. Springholz, Y. Ueta, G. Bauer, and P. J. McCann, Magnetoreflectivity of $Pb_{1-x}Eu_xTe$ epilayers and PbTe/$Pb_{1-x}Eu_xTe$ multiple quantum wells, Phys. Rev. B **55**, 4607 (1997).

[44] G. Grabecki, J. Wróbel, T. Dietl, E. Janik, M. Aleszkiewicz, E. Papis, E. Kamińska, A. Piotrowska, G. Springholz, and G. Bauer, Disorder suppression and precise conductance quantization in constrictions of PbTe quantum wells, Phys. Rev. B **72**, 125332 (2005).

[45] D. W. Pashley, M. J. Stowell, M. H. Jacobs, and T. J. Law, The growth and structure of gold and silver deposits formed by evaporation inside an electron microscope, Philos. Mag. **10**, 127 (1964).

[46] B. B. Haidet, E. T. Hughes, and K. Mukherjee, Nucleation control and interface structure of rocksalt PbSe on (001) zincblende III-V surfaces, Phys. Rev. Mater. **4**, 033402 (2020).

[47] See Supplemental Material at https://link.aps.org/supplemental/10.1103/PhysRevMaterials.7.023401 which includes Refs. [48–50] for information on volume fraction calculation and extended data on surface terracing, pregrowth treatments, AFM, XRD, and TEM.

[48] J. Jung, R. L. M. O. H. Veld, R. Benoist, O. A. H. Molen, C. Manders, M. A. Verheijen, and E. P. A. M. Bakkers, Universal platform for scalable semiconductor-superconductor nanowire networks, Adv. Funct. Mater. **31**, 2103062 (2021).

[49] K. Momma and F. Izumi, VESTA3 for three-dimensional visualization of crystal, volumetric and morphology data, J. Appl. Crystallogr. **44**, 1272 (2011).

[50] J. Als-Nielsen and D. McMorrow, *Elements of Modern X-ray Physics (2nd Edition)* (Wiley, Hoboken, NJ, 2020).

[51] G. Wulff, XXV. Zur Frage der Geschwindigkeit des Wachsthums und der Auflösung der Krystallflächen, Z. Kristallogr.-Crystalline Materials **34**, 449 (1901).

[52] G. D. Barmparis, Z. Lodziana, N. Lopez, and I. N. Remediakis, Nanoparticle shapes by using Wulff constructions and first-principles calculations, Beilstein J. Nanotechnol. **6**, 361 (2015).

[53] P. F. Miceli and C. J. Palmstro/m, X-ray scattering from rotational disorder in epitaxial films: An unconventional mosaic crystal, Phys. Rev. B **51**, 5506 (1995).

[54] E. Bakkers and J. Jung, dataset for "Single-crystalline PbTe film growth through reorientation", doi: 10.5281/zenodo.6900774 (2022).